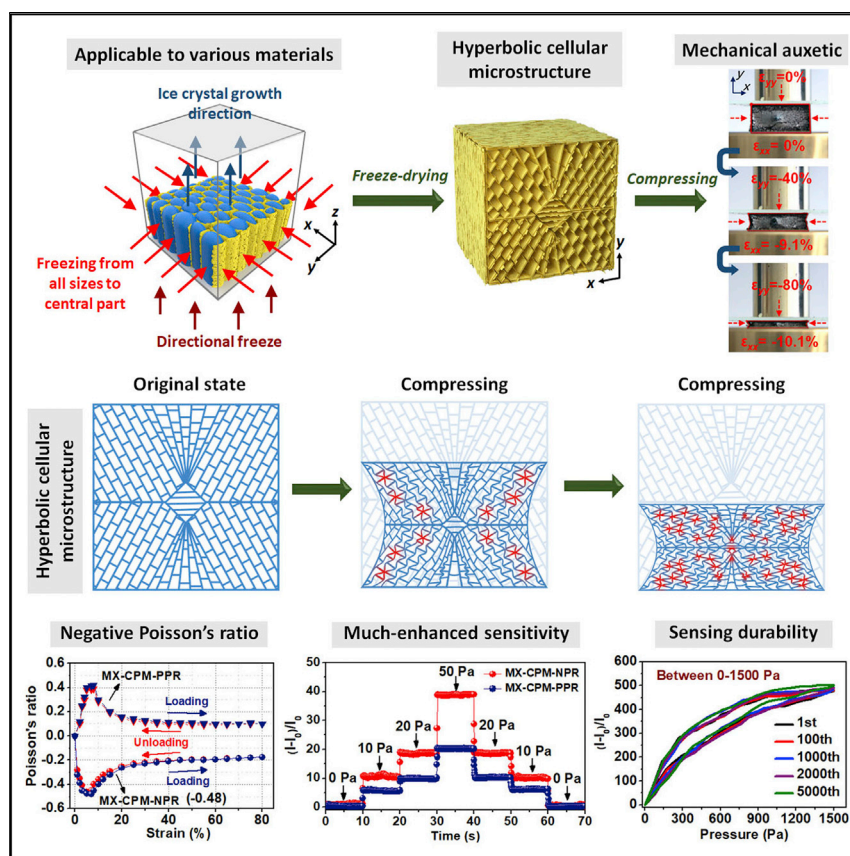


## Article

# An auxetic cellular structure as a universal design for enhanced piezoresistive sensitivity



Shi et al. developed a mechanical strategy to design a conductive porous material (CPM) with an auxetic microstructure and negative Poisson's ratio (NPR) effect to significantly improve the pressure sensing performance of piezoresistive sensors. The proposed mechanical metamaterial strategy was demonstrated to be a facile but effective method for markedly enhancing the pressure sensitivity, sensing durability, and detectable pressure range of piezoresistive sensors.

Xinlei Shi, Yinbo Zhu, Xiangqian Fan, ..., Xinyi Ji, Yongsheng Chen, Jiajie Liang

liang0909@nankai.edu.cn (J.L.)  
wuha@ustc.edu.cn (H.-A.W.)

### Highlights

A mechanical metamaterial strategy to design piezoresistive sensing material

A universal approach to fabricate auxetic cellular structure with NPR

Pressure sensitivity is markedly improved in the meta-structured design



### Improvement

Enhanced performance with innovative design or material control

Shi et al., Matter 5, 1547–1562  
May 4, 2022 © 2022 Elsevier Inc.  
<https://doi.org/10.1016/j.matt.2022.02.022>



## Article

# An auxetic cellular structure as a universal design for enhanced piezoresistive sensitivity

Xinlei Shi,<sup>1,5</sup> Yinbo Zhu,<sup>4,5</sup> Xiangqian Fan,<sup>1,5</sup> Heng-An Wu,<sup>4,\*</sup> Peiqi Wu,<sup>1</sup> Xinyi Ji,<sup>1</sup> Yongsheng Chen,<sup>2</sup> and Jiajie Liang<sup>1,2,3,6,\*</sup>

## SUMMARY

Existing piezoresistive pressure sensors are limited because of the low sensitivity of conventional piezoresistive porous materials, which have positive Poisson's ratio (PPR) values. Here, we propose a universally applicable strategy for fabricating piezoresistive metamaterials with an auxetic cellular structure, negative Poisson's ratio (NPR), and enhanced pressure sensitivity. This hyperbolic and re-entrant microstructure enables porous, conductive metamaterials (e.g., titanium carbide [MXene], graphene, carbon nanotubes, silver nanowire, poly(3,4-ethylenedioxythiophene)/poly(styrenesulfonate) [PEDOT:PSS]) to produce significant macroscopic transverse contraction under longitudinal compression with minimum NPR values below  $-0.45$ . This auxetic effect significantly increases the number of cellular wall-to-wall contact points and conductive pathway formations in the porous metamaterials under compression, significantly reducing electrical resistance. Sensitivity is markedly improved in this design compared with the traditional structure. The substantially enhanced mechanical elasticity and durability induced by the NPR effect gives piezoresistive metamaterials excellent sensing stability and reliability even under repeated episodes of significant compressive deformation.

## INTRODUCTION

Physical activity causes the human body to produce a variety of pressure signals. For instance, small force signals generated from intra-body pressure changes, such as intraocular pressure, intracranial pressure, and internal jugular vein pressure, can provide valuable information regarding the signaler's physiological health status.<sup>1-3</sup> Accurate detection of these force signals is vital for application of pressure sensors in human health monitoring and diagnosis.<sup>1-3</sup> Many researchers have investigated wearable pressure sensors in terms of sensing performance, sensitivity, and durability in recent years. In general, sensing mechanisms that convert changes in external forces into electrical signals for pressure sensors primarily include piezoelectric, piezocapacitive, and piezoresistive effects.<sup>4</sup> Piezoresistive pressure sensors, which are composed of active material placed on a pair of parallel interdigital electrodes or sandwiched between two vertically aligned electrodes, have been intensively investigated for their simple and scalable fabrication processes, easy signal collection, and broad selection of applicable piezoresistive materials.<sup>5</sup> To date, however, few wearable pressure sensor have realized sufficiently high sensitivity ( $>100 \text{ kPa}^{-1}$ ) under low-pressure conditions ( $<1 \text{ kPa}$ ) with long-term cyclic durability for practical applications.<sup>5</sup>

To achieve high sensitivity, piezoresistive materials should be provided with numerous conductive paths for electric current flows and elasticity to withstand

## Progress and potential

A mechanically meta-structured conductive porous material (CPM) with a hyperbolic-like microstructure and negative Poisson's ratio (NPR) was designed and fabricated. Compared with a conventional piezoresistive CPM with a positive Poisson's ratio, key mechanical properties such as elasticity, durability, loading capacity, and indentation resistance were significantly improved in the CMP with NPR behavior. The proposed mechanical metamaterial strategy was demonstrated to be a facile but effective method for markedly enhancing the pressure sensitivity, durability, and detectable pressure range of piezoresistive sensors. This mechanical metamaterial strategy can be regarded as a universally applicable approach for designing highly sensitive piezoresistive materials. This piezoresistive CPM with NPR effect shows great potential for monitoring the physiological health status of the human body.



unexpected and significant mechanical deformation. Conductive porous materials (CPMs), including sponges,<sup>6–8</sup> foams,<sup>9</sup> hollow-sphere films,<sup>10,11</sup> and aerogels,<sup>12–15</sup> have been widely developed because they show high electrical conductivity and good mechanical elasticity. These materials are currently utilized as piezoresistive materials to improve the sensitivity of piezoresistive pressure sensors. However, only a few of the reported sensing devices reach the required sensitivity.<sup>6,14,16</sup> The achievable sensitivity in a low-pressure regimen and the sensing stability under large-scale compressive deformation conditions in wearable pressure sensors made of conventional CPMs are still severely restrained.

Researchers have attempted to optimize sensing properties by focusing on the tuning function or components of CPMs, but few have considered the structural Poisson effect,<sup>17</sup> which determines the strain distribution, structural change, and mechanical properties of materials when they are subjected to deformation.<sup>18,19</sup> In theory, the Poisson's ratio ( $\nu_{xy}$ ) is defined by  $-\epsilon_{xx}/\epsilon_{yy}$ , where  $\epsilon_{xx}$  refers to the transverse strain, and  $\epsilon_{yy}$  is the longitudinal applied strain.<sup>18,19</sup> Conventional elastic CPMs show a positive Poisson's ratio (PPR) value.<sup>20,21</sup> Compression strain compresses a material along the longitudinal direction but expands it in the transverse direction. In the piezoresistive effect, pressure sensitivity is strongly correlated with the quantity of conductive pathways that form in the piezoresistive material.<sup>22,23</sup> Longitudinal compression leads to out-of-plane bending and deformation of the cellular walls in CPMs with a PPR, resulting in increased wall-to-wall contact areas and conduction pathways; transverse expansion has the opposite effect by separating the cellular walls from each other (Figure 1A). As a result, pressure sensitivity triggered by longitudinal compression is offset by transverse expansion in conventional CPMs, which intrinsically restrains their sensitivity.

Unlike conventional natural materials, metamaterials with unique artificially manufactured inner structures can be designed for extraordinary physical properties. Accordingly, they have broad application prospects in the industrial and military fields.<sup>24,25</sup> Particularly, auxetic mechanical metamaterials with a negative Poisson's ratio (NPR) may have unique mechanical performance, including excellent indentation resistance, high loading capacity, large deformability, and superior fracture toughness.<sup>18,19</sup> Figures 1A and 1B illustrate, respectively, the PPR and NPR response for conventional CPMs and meta-structured CPMs under uniaxial compression. Metamaterials with an NPR, unlike those with a PPR, exhibit counterintuitive behavior as they contract in the longitudinal and transverse directions under compression. Benefitting from bidirectional contraction in the metamaterial, CPMs with an NPR can trigger larger volume shrinkage and larger compressive strain in their microstructures.<sup>18</sup> In contrast to conventional PPR behavior, the cellular walls of CPMs with an NPR can buckle or bend out of plane and contract inward, resulting in increased wall-to-wall contact points and more conduction pathways.<sup>23</sup> This can decrease the bulk resistance of meta-structured CPMs under specific compressive strain conditions. Based on this above analysis, we believe that a piezoresistive CPM engineered with an auxetic structure and NPR effect will have high pressure sensitivity.

In this study, we developed a mechanical metamaterial strategy for designing CPMs with an auxetic structure and NPR effect. The proposed metamaterials can contract in the longitudinal and transverse directions under compression. By employing various representative conducting materials as the main building blocks, including 2D nanomaterials of MXene and graphene, 1D nanomaterials of single-walled carbon nanotubes (SWCNT) and silver nanowires (AgNWs), and conducting polymer

<sup>1</sup>School of Materials Science and Engineering, National Institute for Advanced Materials, Nankai University, Tianjin 300350, China

<sup>2</sup>Key Laboratory of Functional Polymer Materials of the Ministry of Education, College of Chemistry, Nankai University, Tianjin 300350, China

<sup>3</sup>Tianjin Key Laboratory of Metal and Molecule-Based Material Chemistry and Collaborative Innovation Center of Chemical Science and Engineering (Tianjin), Nankai University, Tianjin 300350, China

<sup>4</sup>CAS Key Laboratory of Mechanical Behavior and Design of Materials, Department of Modern Mechanics, CAS Center for Excellence in Complex System Mechanics, University of Science and Technology of China, Hefei 230027, China

<sup>5</sup>These authors contributed equally

<sup>6</sup>Lead contact

\*Correspondence:  
liang0909@nankai.edu.cn (J.L.),  
wuha@ustc.edu.cn (H.-A.W.)

<https://doi.org/10.1016/j.matt.2022.02.022>

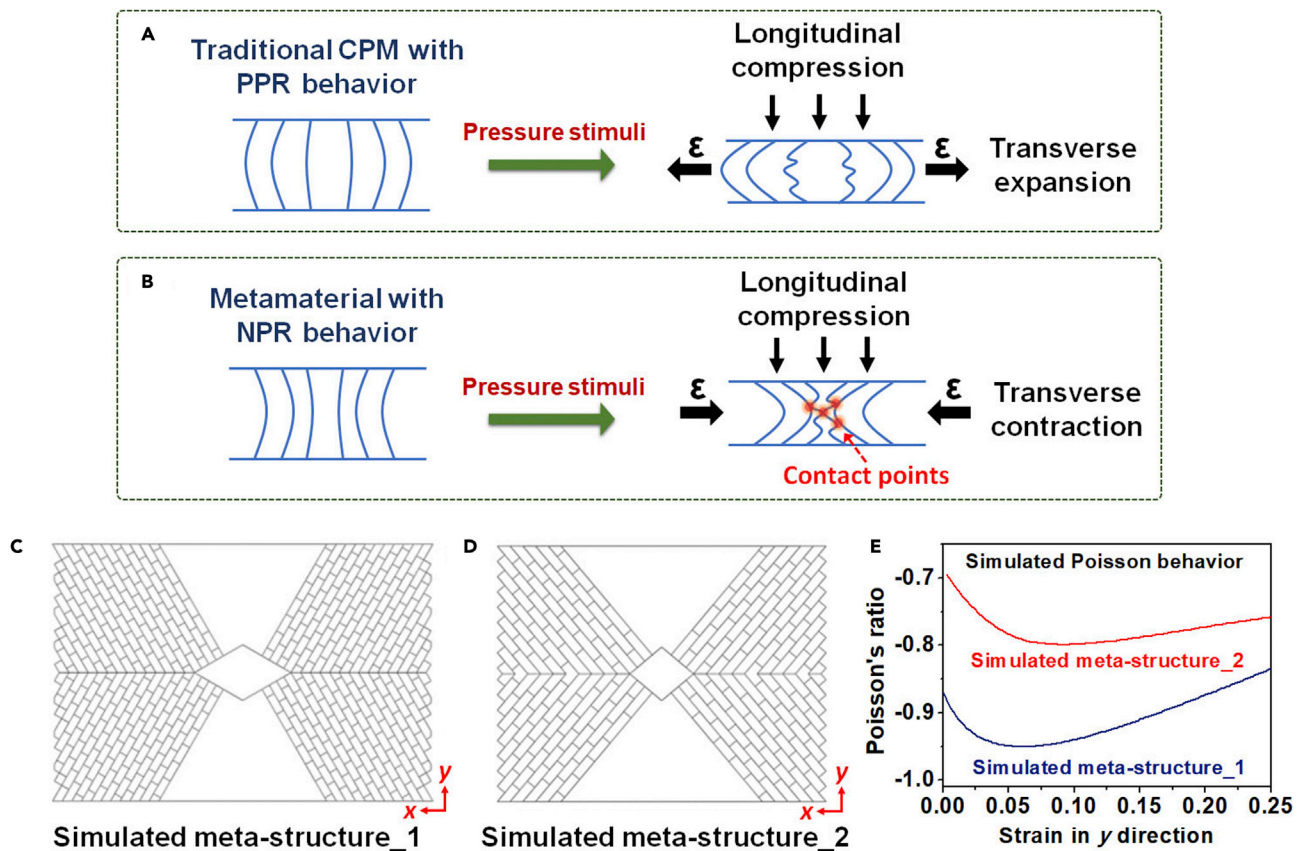


**Figure 1. An auxetic structure with an NPR effect**

(A) Conventional material structure with PPR behavior.

(B) Mechanical metamaterial structure with NPR behavior under uniaxial compression.

(C and D) Meta-structure design of the CPM with a symmetric re-entrant pattern in side parts and a rhombus pattern in the central part (FEA simulation).

(E) Simulated Poisson behavior of simulated meta-structure\_1 and meta-structure\_2. The simulated densities of microcells in the side parts differ in simulated meta-structure\_1 and simulated meta-structure\_2.

PEDOT:PSS, we fabricated a series of auxetic CPMs with hyperbolic re-entrant microstructures using a facile, directional freeze-drying method to create high-performing piezoresistive sensors. Compared with conventional CPMs with a PPR, the pressure sensitivity and sensing durability of all auxetic CPMs are significantly improved because of the marked increase in conductive pathway formation and widely distributed compressive strain induced by the NPR effect. Because the macro-scale properties of metamaterials originate from their microstructures rather than from the material compositions, this mechanical metamaterial strategy can be regarded as a universally applicable approach for designing highly sensitive piezoresistive materials.

## RESULTS AND DISCUSSION

### Designing a piezoresistive CPM with an auxetic porous structure

The NPR effect of metamaterials primarily depends on their geometry or microstructure.<sup>18,24–28</sup> This micro-scale topology of metamaterials can be tailored to produce specific mechanical or physical properties.<sup>29,30</sup> Three main classes of auxetic structures—re-entrant, chiral, and rotating rigid—have been realized in the construction of metamaterials with NPR.<sup>31</sup> Among them, the re-entrant structure is the most widely investigated auxetic structure because of its relative simplicity in the

manufacturing process. To prepare a piezoresistive metamaterial with bidirectional contraction, we first employed finite element analysis (FEA) methods to design an auxetic porous structure with a symmetric hyperbolic re-entrant pattern in the side parts and a rhombus pattern in the central part to obtain large NPR deformation (Figures 1C and 1D).<sup>19</sup> Under compression along the y direction, displacement was applied to the top boundary of the FEA model, and the bottom boundary was fixed by hinge constraints.

The Poisson's ratio values were calculated as the ratio of lateral shrinking strain to vertical compressive strain. The Poisson's ratio curves of the designed model were found to fall into the negative region and to be concave downward with a minimum value, as shown in Figure 1E. The purpose of the rhombus pattern at the center is to cushion the shrinking deformation of the re-entrant cellular pattern. This NPR behavior is strongly dependent on the structural parameters of the CPM, including the shape of the re-entrant and rhombus patterns in the central part (Figure S1) and the microcell density in the side part (Figures 1C and 1D).<sup>18</sup> This re-entrant design ensures significant transverse shrinkage under longitudinal compression in the CPM.

#### Fabrication and characterization of a piezoresistive CPM with an NPR

We used a directional freeze-drying method to fabricate piezoresistive CPM monoliths with the target auxetic meta-structure based on homogeneous aqueous mixtures of a range of representative conductive materials as precursors (Figures 2A and S2), including 2D nanomaterials of MXene and graphene, 1D nanomaterials of SWCNTs and AgNWs, and conducting polymer PEDOT:PSS (Figure S3). We prepared the MXene-based CPM with an auxetic structure and NPR effect (MX-CPM-NPR) as an example through a facile three-step process involving hydrothermal reaction, directional freezing, and freeze-drying. The fabricated MX-CPM-NPR has a homogeneous mixture of  $\text{Ti}_3\text{C}_2\text{T}_x$  MXene nanosheets and 3-glycidoxypropyltrimethoxysilane (GPTMS) suspension as the raw materials. 2D MXene was selected because of its high electrical conductivity, good mechanical flexibility, and rich surface functional groups.<sup>26,32</sup> Pure MXene CPM typically has weak mechanical properties, so GPTMS was chosen as a cross-linking material to enhance the mechanical strength of the MXene-based CPM.<sup>33–37</sup> Under a hydrothermal reaction, GPTMS was initially hydrolyzed to produce a hydrolyzed siloxane that can undergo a condensation reaction with Ti-OH groups on the surface of MXene nanosheets to form a cross-linked network.<sup>35–37</sup> The solution was poured into an open-topped container and placed under a bidirectional cold source to ensure anisotropic ice crystallization in the transverse and longitudinal directions (Figures 2A and S2). Finally, the MX-CPM-NPR monolith was obtained by freeze-drying.

This directional freeze-drying process is a general but useful approach for fabricating CPMs with auxetic re-entrant microstructures regardless of building blocks. Other meta-structured CPMs with NPR behavior are made of graphene (GR-CPM-NPR), SWCNTs (CNT-CPM-NPR), AgNWs (AG-CPM-NPR), and PEDOT:PSS (PP-CPM-NPR). For comparison, conventional CPMs with disordered porous structures and PPR behavior based on MXene (MX-CPM-PPR), graphene (GR-CPM-PPR), SWCNTs (CNT-CPM-PPR), AgNWs (AG-CPM-PPR), and PEDOT:PSS (PP-CPM-PPR) were also fabricated (details are given below).

Although the MX-CPM-PPR monolith exhibits isotropic electrical conductivity ( $\sim 4.6$  S/m), the MX-CPM-NPR monolith shows anisotropic electrical conductivity (with  $\sim 2.7$  S/m along the x direction,  $\sim 1.8$  S/m along the y direction, and  $\sim 12$  S/m along the z direction), which can be attributed to its anisotropic porous structure. Scanning

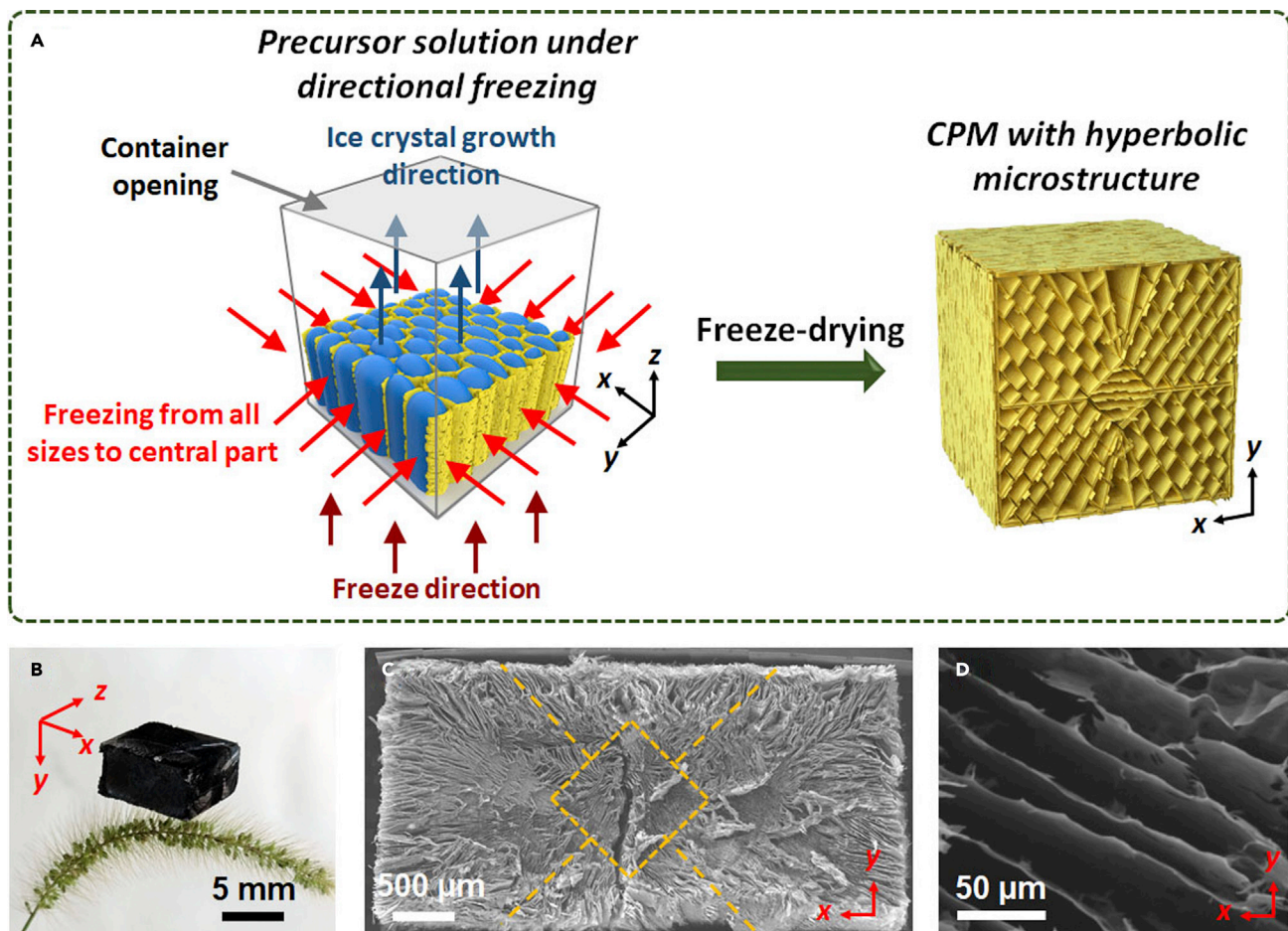


**Figure 2. Meta-structure preparation and characterization**

(A) Schematic of fabrication of the CPM with a hyperbolic microstructure using the directional freeze-drying process.

(B) A photograph showing an MX-CPM-NPR monolith sitting atop green bristlegrass.

(C) Entire SEM image in x-y cross-section of the MX-CPM-NPR monolith, revealing a hyperbolic porous side part and rhombic disordered porous central part.

(D) Magnified SEM image showing the sunflower seed-like microcells in the re-entrant side part of MX-CPM-NPR.

electron microscopy (SEM) characterizations from the x-y cross-section show that MX-CPM-NPR is composed of various sunflower seed-like microcells that are assembled into two patterns in the scaffold: a hyperbolic re-entrant porous side part and a rhombic disordered porous central part (Figures 2C and 2D). This hyperbolic MX-CPM-NPR microstructure is analogous to the designed auxetic structure with a significant NPR, as shown in Figures 1C and 1D. Microcells in the hyperbolic side part larger, with a maximum cellular wall length ( $l$ ) approaching  $\sim 1,300 \mu\text{m}$  (Figure 2C); microcells in MX-CPM-PPR are smaller in size, with  $l$  varying from 200–500  $\mu\text{m}$  (Figure S4). Other meta-structured CPMs, including CNT-CMP-NPR, AG-CMP-NPR, GR-CMP-NPR, and PP-CMP-NPR, have hyperbolic microstructures similar to that of MX-CPM-NPR (Figure S5).

### Mechanical properties of CPMs with an NPR

The piezoresistive effects of sensing materials are strongly dependent on their mechanical features. We compared the compressive mechanical properties of the CPMs through a quasi-static uniaxial compression-release test in the y-y direction (Figure 3A). The monolithic MX-CPM-NPR demonstrated high recoverability under

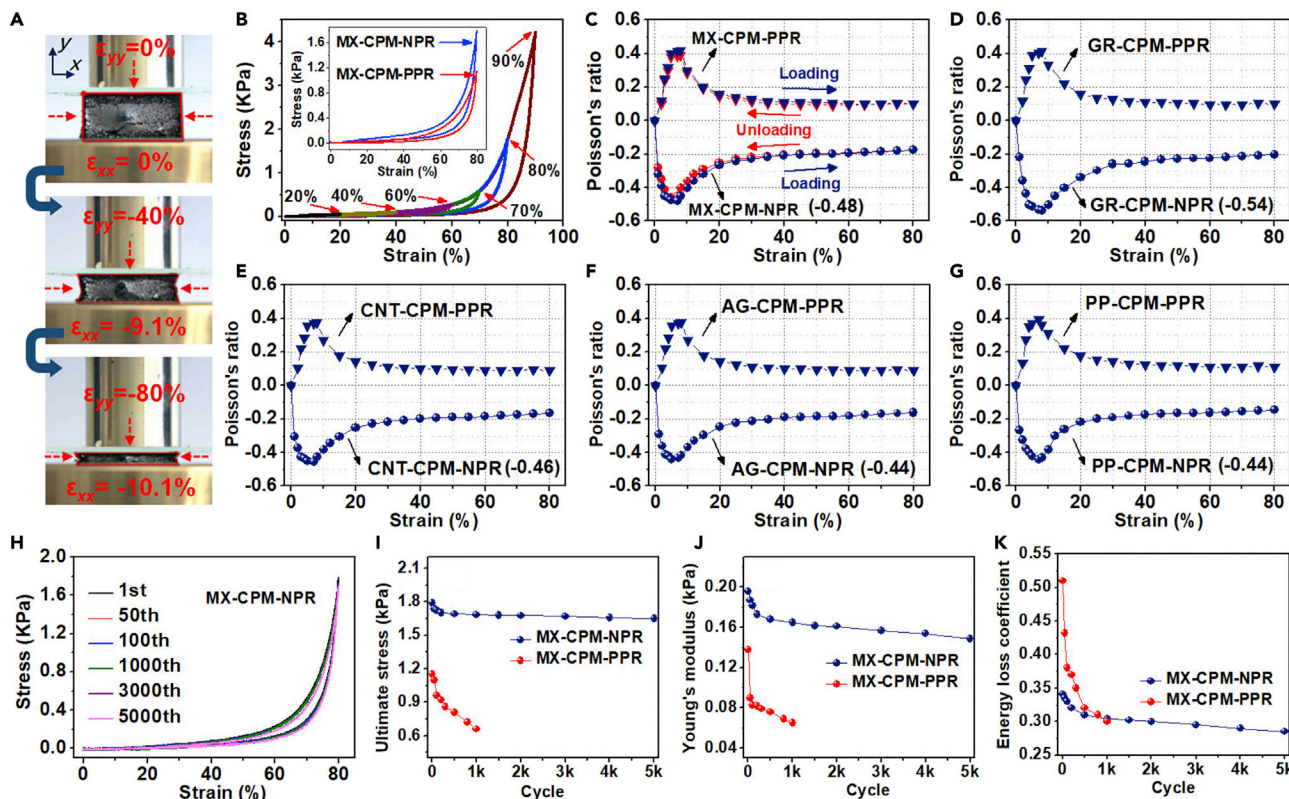


**Figure 3. Mechanical properties of meta-structured CPMs**

(A) Photographs of the x-y cross-sectional views of transverse contraction and NPR behavior of the MX-CPM-NPR monolith under uniaxial compression. (B) Compressive stress-strain curves during compression-release cycles for MX-CPM-NPR with various maximum strains of up to 90% (inset: compressive stress-strain curves of MX-CPM-NPR versus MX-CPM-PPR with strain up to 80%); (C) Evolution of Poisson's ratio as a function of compressive strain ( $\epsilon_{yy}$ ) in 1 compression-release cycle with maximum strain of 80% for MX-CPM-NPR and MX-CPM-PPR. (D–G) Evolution of Poisson's ratio for GR-CPM-NPR and GR-CPM-PPR (D), CNT-CPM-NPR and CNT-CPM-PPR (E), AG-CPM-NPR and AG-CPM-PPR (F), and PP-CPM-NPR and PP-CPM-PPR (G) with strain up to 80%. (H) Compressive stress-strain curves at 80% maximum strain over 5,000 compression-release cycles for MX-CPM-NPR. (I–K) Changes in ultimate stress, Young's modulus, and energy loss coefficient of MX-CPM-NPR and MX-CPM-PPR during continuous compression-release cycles at 80% maximum strain.

uniaxial compression-release cycles, with only a small residual strain (less than 1%) observed in the first compression-release cycle at a maximum strain of 90% (Figure 3B). As expected, the MX-CPM-NPR sample showed macroscopic hyperbolic-shaped shrinkage and strong contraction behavior in the x-x direction when longitudinal stress was applied in the y-y direction during the compression test (Figure 3A). The bending degree of the hyperbolic patterns in the microstructure increased, and the strain of  $\epsilon_{xx}$  monotonically decreased to  $-10.1\%$  as  $\epsilon_{yy}$  decreased to  $-80\%$  (Figure 3A), indicating NPR behavior in MX-CPM-NPR under longitudinal compression.

The Poisson's ratio value determined by  $-\epsilon_{xx}/\epsilon_{yy}$  showed a negative response across the entire compressive strain range, with two continuous regions: first decreasing to a peak value of  $-0.48$  as  $\epsilon_{yy}$  decreased to  $-7\%$  and then gradually increasing to  $-0.175$  with further decrease in  $\epsilon_{yy}$  to  $-80\%$  (Figure 3C). This NPR response agrees well with the simulated data obtained for the designed meta-structure (Figure 1E). Similar to MX-CPM-NPR, the other meta-structured CPMs based on graphene, SWCNTs, AgNWs, and PEDOT:PSS exhibited NPR behavior over the

whole compressive strain range with peak values smaller than  $-0.45$  (Figures 3D–3G). The Poisson's ratio values of MX-CPM-PPR, GR-CPM-PPR, CNT-CPM-PPR, AG-CPM-PPR, and PP-CPM-PPR with conventional porous structures exhibited positive responses across the entire compressive strain range, with maximum peak values exceeding 0.4 (Figures 3C–3G).

NPR behavior can lead to higher shrinkage volume and wider compressive strain distribution in the microstructure,<sup>18</sup> so MX-CPM-NPR exhibits better indentation resistance and loading capacity than MX-CPM-PPR (Figure 3B, inset). Because the pressure sensitivity of the CPM sensor is inversely proportional to the Young's modulus ( $E$ ) of the materials, a low mechanical modulus is also required for the material to achieve high mechanical sensitivity.<sup>3</sup> As shown in Figure S6, the Young's modulus ( $E$ ) of the MX-CPM-NPR sample was scaled with relative density  $\rho_s$  as  $E \sim \rho_s^m$  with the exponent  $m = 1.675$ . The exponent  $m$  represents the geometrically mechanical response of a cellular structure exhibiting stretching-dominated behavior ( $m = 1$ ) or bending-dominated behavior ( $m > 2$ ).<sup>19</sup> This scaling response with  $m = 1.675$  suggests that MX-CPM-NPR deforms predominantly in a mixed mode of stretching and bending in the microstructure, which enhances strength and flexibility.<sup>19</sup> The compressive modulus of MX-CPM-NPR was calculated from the linear elastic region of the stress-strain curves. The monolith with a density of  $\sim 10 \text{ mg/cm}^3$  has an extremely low value of about 200 Pa, indicating soft characteristics.<sup>12,38,39</sup>

The energy loss coefficient of the MX-CPM-NPR aerogel calculated from the small hysteresis loop in the stress-strain curve is as low as 0.34, which is much lower than that of MX-CPM-PPR (0.51) and is one of the lowest energy loss coefficients among reported elastic aerogel materials (Table S1). A low energy loss coefficient indicates low energy dissipation during the compression-release process, which is conducive to reliable sensing applications.<sup>40</sup>

Super-elasticity also plays a critical role in stabilizing the sensing performance of the aerogel sensor. The CPM samples were subjected to dynamic compression-release cycles with a compressive strain of up to 80% (Figures 3H and S7). The MX-CPM-NPR monolith outperformed MX-CPM-PPR in terms of compressive elasticity. The auxetic metamaterial demonstrates only slight degradations of 8%, 24%, and 16% in terms of ultimate stress, Young's modulus, and energy loss coefficient mechanical properties, respectively, after 5,000 cycles (Figures 3I–3K). This metamaterial appears to perform extremely well in terms of compressive elasticity and durability among the reported CPMs to date (Table S1). In contrast, the ultimate stress, Young's modulus, and energy loss coefficient values of MX-CPM-PPR decreased by at least 40% after being compressed for 1,000 cycles with 80% maximum strain.

Compared with previously reported CPMs and MX-CPM-PPR, our MX-CPM-NPR exhibits ideal comprehensive mechanical properties as a high-performing piezoresistive sensing material, including super-elasticity, ultra-softness, a low energy loss coefficient, and a long cycle lifespan. These intriguing mechanical features can be attributed to the auxetic meta-structure ensures widely distributing compressive strain under mechanical excitations, which gives CPM superior deformability and fracture toughness to withstand large compressive deformation.<sup>18,19</sup> Upon compression, bending or buckling of the cellular walls allows them to store a large portion of applied energy in the porous meta-structures.<sup>40</sup> Chemical cross-linking between GPTMS and MXene nanosheets also makes MXene-based cellular walls much stronger and tougher, preventing them from concentrating stress or breaking off.<sup>34</sup>

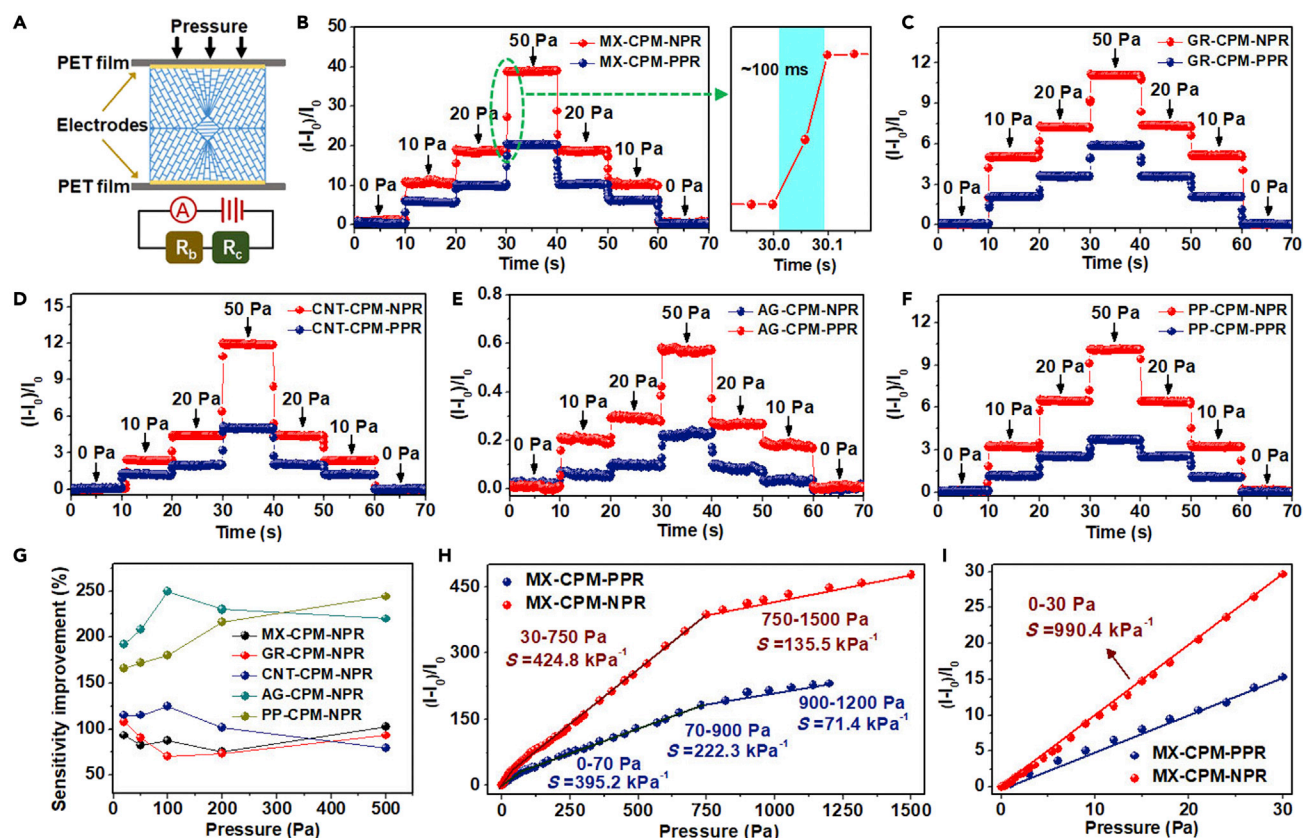


**Figure 4. Pressure sensitivity of CPM sensors**

(A) Schematic of the structure of the piezoresistive pressure sensor.

(B) Relative current changes in MX-CPM-NPR and MX-CPM-PPR sensors in response to gradient pressure (0–50 Pa) with time (right: magnified curve of transient sensing response time to applied pressure for MX-CPM-NPR).

(C–F) Relative current changes over time for GR-CPM-NPR and GR-CPM-PPR sensors (C), CNT-CPM-NPR and CNT-CPM-PPR sensors (D), AG-CPM-NPR and AG-CPM-PPR sensors (E), and PP-CPM-NPR and PP-CPM-PPR sensors (F) to gradient pressure (0–50 Pa).

(G) The improvement of relative current changes under specific pressure for piezoresistive CPMs with an NPR compared with CPMs with a PPR.

(H) Relative current changes and pressure sensitivity of MX-CPM-NPR and MX-CPM-PPR sensors over the entire pressure range.

(I) Pressure sensitivity of MX-CPM-NPR and MX-CPM-PPR sensors below 30 Pa.

### Enhancement of sensing performance for CPMs with an NPR

To assess their pressure-sensing properties, CPMs were assembled into piezoresistive pressure sensors by sandwiching the monolithic samples between two flexible silver-coated poly(ethylene terephthalate) (PET) sheets with the electrode films parallel to the x-z plane of the monolith (Figure 4A). The resulting square pressure-sensitive pad was  $1 \times 1$  cm in size. An equivalent resistance model was first established to access the sensing mechanism of the CPM-based sensing device based on changes in resistance derived from the density variations of the cellular wall-to-wall contacting points ( $R_c$ ) as well as the bending or buckling of cellular walls ( $R_b$ ). External pressure applied to the CPM sensor was detected based on the total resistance change ( $R_T$ ) evidenced by  $R_c$  and  $R_b$  (Figure 4A).

Figure 4B shows the dependence of time-resolved relative current changes  $(I-I_0)/I_0$ , where  $I$  is the initial current and the responsive current under certain applied pressure) on the various pressure stimuli of MX-CPM-NPR and MX-CPM-PPR sensors. The MX-CPM-NPR sensor shows much larger relative current changes than the MX-CPM-PPR sensor under the same pressure stimuli. The MX-CPM-NPR sensor shows a short

response/recovery time (Figure 4B, right) and stable stepped responsive current changes, demonstrating rapid sensing capability, high sensing resolution, and excellent sensing robustness. The relative current changes under specific applied pressure in other piezoresistive CPMs based on graphene, SWCNTs, AgNWs, and PEDOT:PSS are shown in Figures 4C–4F. Similar to the MX-CPM-NPR sensor, these meta-structured CPMs show significant improvements in relative current change compared with their counterparts with conventional PPR behavior. For instance, PP-CMP-NPR shows approximately 160%, 170%, 180%, 210%, and 240% enhancement in relative current change under specific pressures of 20, 50, 100, 200, and 500 Pa, respectively, compared with PP-CMP-PPR (Figure 4G). This enhancement is closely related to the auxetic structure and NPR effect.

According to the relationship between the output current signals and the applied pressure stimuli, the calibrated curves of relative current changes over different pressure ranges for CPM-based sensing devices are shown in Figures 4H and S8. The sensing curves for MX-CPM-NPR and MX-CPM-PPR sensors under the full pressure range were divided into three fitting lines with progressively decreasing slopes: a low-pressure regimen of 0–30 Pa with linearity of 0.998, a medium-pressure regimen of 30–750 Pa with linearity of 0.996, and a high-pressure regimen of 750–1,500 Pa with linearity of 0.985 for the MX-CPM-NPR sensor, in addition to a low-pressure regimen of 0–70 Pa with linearity of 0.98, a medium-pressure regimen of 70–900 Pa with linearity of 0.991, and a high-pressure regimen of 900–1,200 Pa with linearity of 0.981 for the MX-CPM-PPR sensor. The MX-CPM-NPR sensor shows a significantly steeper increase in the relative current change curve over the full pressure range than the MX-CPM-PPR sensor (Figures 4H and 4I). Similar phenomena were also observed in other meta-structured CPMs and their counterparts with conventional structures (Figure S8).

The pressure sensitivity ( $S=(I-I_0)/I_0/\Delta P$ , where  $\Delta P$  is applied pressure) of the MX-CPM-NPR sensor was calculated at up to  $990.4 \text{ kPa}^{-1}$  under pressure below 30 Pa (Figure 4I), which is much higher than that of MX-CPM-PPR ( $395.2 \text{ kPa}^{-1}$  below 70 Pa) and exceeds the highest sensitivity of most piezoresistive pressure sensors achieved previously (Table S2).<sup>10,12–16,41–45</sup> Sensitivity decreases slightly to  $424.8 \text{ kPa}^{-1}$  and  $135.5 \text{ kPa}^{-1}$  in the subsequent medium- and high-pressure linear ranges, respectively, but these values are still excellent in terms of other pressure sensors reported to date (Table S2). In addition to having a smaller maximum pressure limit, the MX-CPM-PPR sensor shows much lower pressure sensitivity than the MX-CPM-NPR sensor over the full pressure range as well. GR-CPM-NPR, CNT-CPM-NPR, AG-CPM-NPR, and PP-CPM-NPR sensing devices all showed significant increases in pressure sensitivity across the entire applied pressure range compared with GR-CPM-PPR, CNT-CPM-PPR, AG-CPM-PPR, and PP-CPM-PPR, respectively (Figure S8). These results indicate that the proposed mechanical metamaterial strategy is a universally applicable method for enhancing the pressure sensitivity of piezoresistive materials.

The sensing mechanism for piezoresistive MX-CPM-NPR is dominated by three stages of geometric deformation in the microcells (Figure 5A): bending and buckling of cellular walls in microcells located on the hyperbolic side part of the CPM in a low-pressure regimen of 0–30 Pa (Figure 5B), bending and buckling of cellular walls in microcells located on the amorphous central part of the CPM in a medium-pressure regimen of 30–750 Pa (Figure 5C), and densification of all microcells in a high-pressure regimen of 750–1,500 Pa.<sup>46</sup> When pressure is below 30 Pa (corresponding to a compressive strain  $\epsilon_{yy}$  below  $-22\%$ ), the MX-CPM-NPR monolith first exhibits a rapid

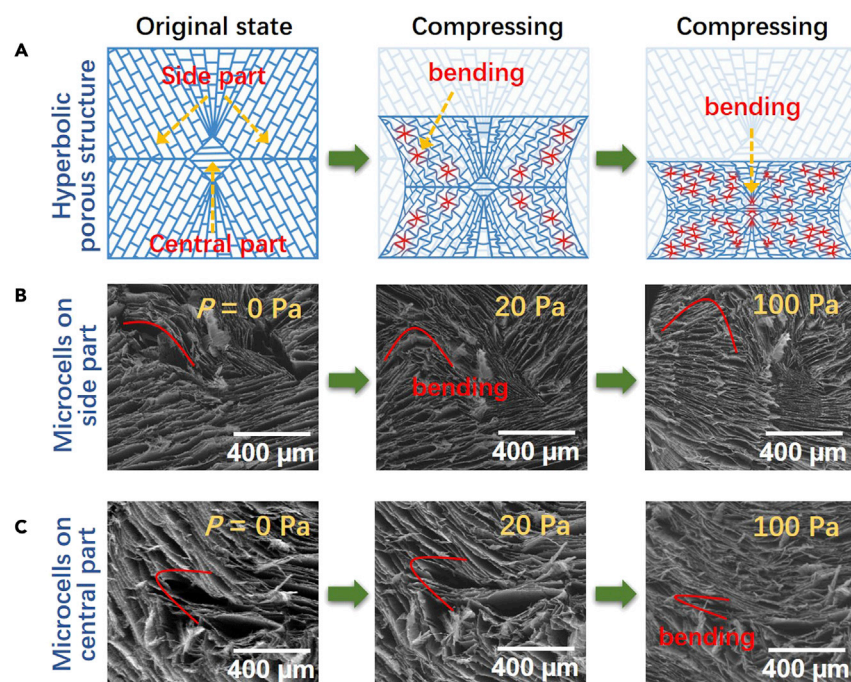


**Figure 5. Sensing mechanism**

(A) Illustration of the sensing mechanism of MX-CPM-NPR.

(B and C) SEM images showing the bending process of cellular walls in microcells located in (B) the side part and (C) the central part of the MX-CPM-NPR sensor upon applied pressure of 0 Pa, 20 Pa (low-pressure regimen), and 100 Pa (medium-pressure regimen), respectively.

decrease in Poisson's ratio and produces a maximum NPR of  $-0.48$  at about  $3.6$  Pa (corresponding to  $\varepsilon_{yy}$  of  $-7\%$ ) and then shows a relatively mild increase toward a negative NPR value of  $-0.25$  at about  $30$  Pa (corresponding to  $\varepsilon_{yy}$  of  $-22\%$ ). This large NPR indicates significant hyperbolic-shaped shrinkage in the macroscopic configuration and significant contraction in the microstructure in both transverse directions, which induces more cellular wall-to-wall contact points and conduction pathways in the microstructure of the compressed CPM. These phenomena significantly decrease electrical resistance while increasing the sensitivity of the piezoresistive sample's meta-structure. In the medium-pressure range ( $30$ – $750$  Pa), bending and buckling of microcells located on the disordered central part begins to dominate the structural deformation of the CPM. The steady NPR behavior from  $30$ – $750$  Pa (corresponding to  $\varepsilon_{yy}$  from  $-22\%$  to  $-73.5\%$ ) may originate from a trade-off in the microcell deformation in the disordered central part and re-entrant side parts.

The long cycle life reflects the material's ability to retain electrical function and structural integrity under long-term cyclic compression-release cycling, which is vital for pressure-sensing materials. To evaluate the sensing durability and stability of MX-CPM-NPR, the sensing devices were subjected to cyclic compression-release between  $0$ – $10$  Pa and  $0$ – $1500$  Pa. The output currents of the MX-CPM-NPR sensors were well maintained throughout  $5,000$  cycling tests (Figures 6A and 6B). The specific isolated sensing curves at the first, 100th, 1,000th, 2,000th, and 5,000th compression-release cycles coincide (Figure 6D), confirming the good monotonicity and long-term durability of the MX-CPM-NPR sensor even under large, repeated episodes of structural deformation. In contrast, the control device of the MX-CPM-PPR

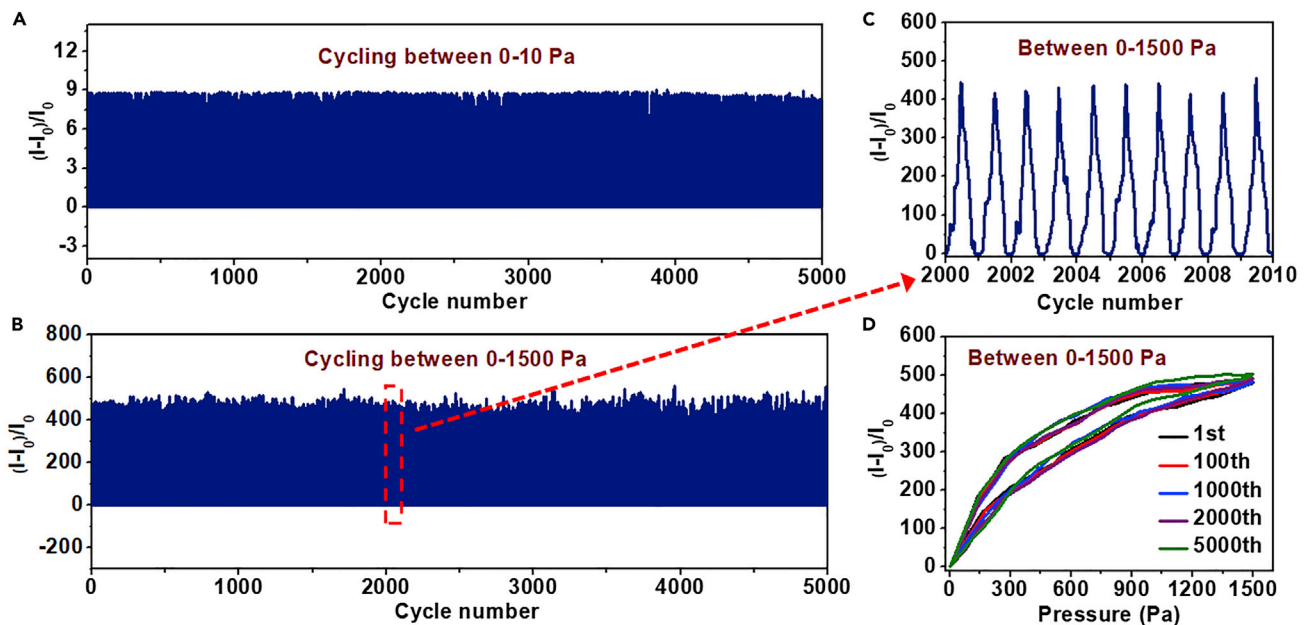


**Figure 6. Sensing durability of the MX-CPM-NPR sensor**

(A and B) Relative current changes of the MX-CPM-NPR sensor over 5,000 compression-release cycles with maximum pressure of (A) 10 Pa and (B) 1500 Pa.

(C) Detailed relative current change curves recorded between 2,000 and 2,010 compression-release cycles at 1,500 Pa.

(D) Detailed relative current changes versus pressure curves at the first, 100th, 1,000th, 2,000th, and 5,000th compression-release cycles (1,500 Pa).

sensor showed a significant decrease in the peak value of the current changes after 1,000 compression-release cycles with a maximum pressure of 500 Pa (Figure S9), indicating relatively poor cycling stability.

In addition to significantly improved pressure sensitivity and sensing durability, meta-structured CPMs with hyperbolic re-entrant microstructures showed significant enhancement in the maximum detectable pressure range (Figures 4H and S8). This is because CPMs with an NPR have a better indentation resistance and force loading capacity compared with their PPR structure counterparts, which is consistent with their mechanical properties (Figure 3B). The robust compression-release cyclability and sensing durability of MX-CPM-NPR sensors are closely correlated with their mechanical elasticity and cyclic compression-release stability as derived from the hyperbolic meta-structure.

The radial artery pulse of a human male subject was monitored to demonstrate practical application of the proposed piezoresistive CPM with an auxetic microstructure and NPR effect. Two wearable pressure sensors, made of MX-CPM-PPR and MX-CPM-NPR, were attached separately to the skin of the volunteer's wrist, as shown in the inset in Figure 7A. The piezoresistive CPMs with conventional PPR behavior and NPR effect detected the waveform signals from the radial artery pulse (Figures 7A and 7B), but only the MX-CPM-NPR sensor could isolate the radial wave of a single heartbeat, distinguishing the characteristic peaks related to the forward wave, peak systolic pressure, diastolic notch, and tricuspid valve opening because of its very high sensitivity (Figure 7D).<sup>17</sup> The MX-CPM-PPR pressure sensor provided only one relatively weak and broad peak signal within a single heartbeat, losing the important characteristic peaks associated with valuable clinical information (Figure 7C) because of its relatively low sensitivity. These results indicate that the piezoresistive CPM with an auxetic microstructure and NPR effect can continuously detect pulse blood

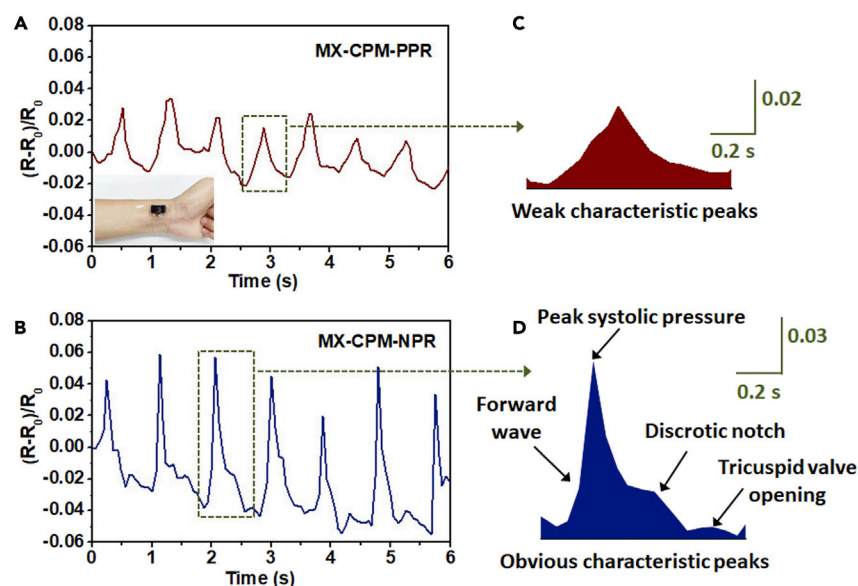


**Figure 7. Human radial pulse monitoring via the MX-CPM-NPR and MX-CPM-PPR sensors**  
 (A and B) Relative resistance variation of wrist pulse detected by the MX-CPM-PPR (A) and MX-CPM-NPR sensors (B). The inset in (A) shows the wearable pressure sensor attached to a human wrist.  
 (C and D) Enlarged signals from the MX-CPM-PPR (C) and MX-CPM-NPR sensors (D) show detailed characteristic peaks within a single heartbeat.

pressure waveforms to accurately monitor the physiological health status of the human body.

## Conclusions

We developed a mechanical strategy to design CPMs with auxetic microstructures and NPR effect to significantly improve the pressure sensing performance of piezoresistive sensors. Compared with conventional CPMs with a PPR that exhibit transverse expansion upon longitudinal compression, the meta-structured CPM contracts in the longitudinal and transverse directions under compression because of its re-entrant design. The NPR effect causes the cellular walls of the meta-structured CPM to buckle or bend out of plane while contracting inward in response to compression stimuli, which increases wall-to-wall contact points and conduction pathways. Compared with the conventional CPM, key mechanical properties related to elasticity, durability, loading capacity, and indentation resistance were significantly improved in the CMP with NPR behavior. The proposed mechanical metamaterial strategy was demonstrated to be a facile but effective method for markedly enhancing the pressure sensitivity, sensing durability, and detectable pressure range of piezoresistive sensors. Because negative-index properties primarily depend on artificial microstructures rather than material components, improving the piezoresistive sensing performance at the metamaterial level can be regarded as a universal approach to designing a wide range of micro-structured and porous piezoresistive sensing materials.

## EXPERIMENTAL PROCEDURES

### Resource availability

#### Lead contact

Further information and requests for resources and materials should be directed to, and will be fulfilled by, the lead contact, Jiajie Liang ([liang0909@nankai.edu.cn](mailto:liang0909@nankai.edu.cn)).

#### Materials availability

This study did not generate new unique reagents.

#### Data and code availability

This study did not generate or analyze datasets or code.

#### Raw materials

Titanium aluminum carbide ( $\text{Ti}_3\text{AlC}_2$ ) was purchased from 11 Technology (China). GPTMS was purchased from Meryer Chemical Technology (Shanghai, China). Graphene oxide (GO) was prepared from graphite following the modified Hummers method.<sup>47</sup> AgNWs were purchased from Nanjing XFNANO Materials Tech. PEDOT:PSS was purchased from Heraeus (Shanghai, China). SWCNT solution was purchased from OCSiAl Technology.

#### Synthesis of $\text{Ti}_3\text{C}_2\text{T}_x$ nanosheets

Titanium carbide ( $\text{Ti}_3\text{C}_2\text{T}_x$ ) MXene was prepared by selective etching of aluminum from  $\text{Ti}_3\text{AlC}_2$  (400 mesh size) and delamination using the minimally intensive layer delamination (MILD) method. First, lithium fluoride (2 g) and hydrochloric acid (40 mL, 9 mol/L) were stirred together for 30 min. Then  $\text{Ti}_3\text{AlC}_2$  (1 g) was added to the solution. The mixture was heated at 35°C, stirred for 24 h, and then poured into a centrifuge tube for centrifugation at 3,500 rpm for 10 min. The supernatant was removed, and deionized (DI) water was added until the pH of the supernatant exceeded 5. The bottom precipitated  $\text{Ti}_3\text{C}_2\text{T}_x$  layer was dispersed into ethanol with ultrasonication for 30 min. The ethanol was then removed by centrifugation at 10,000 rpm for 30 min. DI water was added to the remaining precipitate, and after centrifugation at 3,500 rpm, a uniform  $\text{Ti}_3\text{C}_2\text{T}_x$  suspension was formed. Finally, MXene powder was obtained by freeze-drying the homogeneous  $\text{Ti}_3\text{C}_2\text{T}_x$  MXene solution.

#### Preparation of MX-CPM-NPR

First,  $\text{Ti}_3\text{C}_2\text{T}_x$  MXene powder was evenly dispersed into water by ultrasound to form a 10 mg/mL aqueous dispersion. GPTMS was added to the dispersion with ultrasound for 10 min; the mass ratio of MXene to GPTMS was 5:1. The obtained dispersion was sealed in a hydrothermal reactor and subjected to a hydrothermal reaction at 80°C for 1 h. The dispersion was poured into a glass tube and placed in a bidirectional cold source, which was controlled by a customized hemispherical Dewar bottle. The bottom of the Dewar bottle was supplied with liquid nitrogen as a cold source, and the top used room temperature as a heat source, forming a first bottom-up temperature gradient in the vertical direction. A piece of copper was placed at the liquid level of the liquid nitrogen as a platform, then the container containing the solution was placed onto it. A second temperature gradient direction then formed from the outside to the inside of the container, with the cooler four sides as the cold source and the inside of the sample as the heat source. After 10 min, the solution was completely frozen. The container was placed in the freeze dryer for 5 days until the ice crystals were completely removed. Finally, the material was heated in an argon environment at 200°C for 2 h to obtain final MX-CPM-NPR monoliths.

#### Preparation of MX-CPM-PPR

First, a 10 mg/mL MXene solution was prepared by dispersing powder-like  $\text{Ti}_3\text{C}_2\text{T}_x$ -MXene in DI water via oscillation. The designated amount of GPTMS was added to the solution with oscillation for 10 min. The mass ratio of MXene to GPTMS was 5:1. The solution was sealed in a hydrothermal reactor and heated for 1 h at 80°C, poured into a container, and placed into a -3°C freezer for 5 h until the solution was

completely frozen. A PPR structure eventually formed via contribution of a uniform cold field provided by the cold source. After 5 days of freeze-drying, the ice crystals in the sample were volatilized completely, and the sample was removed from the container. The sample was placed in a tube furnace for calcination at 200°C in an argon atmosphere for 2 h to obtain MX-CPM-PPR.

#### Preparation of CNT-CPM-NPR and CNT-CPM-PPR

SWCNT aqueous dispersion was diluted to 4 mg/mL and poured into a glass tube. The subsequent freeze-drying process of SWCNT-based CPMs with an NPR and PPR was the same as that of MXene-based CPMs. Piezoresistive samples were obtained after the freeze-drying process was complete.

#### Preparation of PP-CPM-NPR and PP-CPM-PPR

PEDOT:PSS aqueous solution with a concentration of 14 mg/mL was poured into a glass tube. The subsequent freeze-drying process of PEDOT:PSS-based CPMs with an NPR and PPR was the same as that of MXene-based CPMs. Piezoresistive samples were obtained after the freeze-drying process was complete.

#### Preparation of AG-CPM-NPR and AG-CPM-PPR

AgNW aqueous solution with a concentration of 10 mg/mL was poured into a glass tube. The subsequent freeze-drying process of AgNW-based CPMs with an NPR and PPR was the same as that of MXene-based CPMs. Piezoresistive samples were obtained after the freeze-drying process was complete.

#### Preparation of GR-CPM-NPR and GR-CPM-PPR

GO powder was evenly dispersed in water by ultrasound for 1 h to form a 4 mg/mL aqueous dispersion. The dispersion was poured into a glass tube. The subsequent freeze-drying process of reduced GO-based CPMs with an NPR and PPR was the same as that of MXene-based CPMs. After the freeze-drying process, the samples were placed in a culture dish, and 5 mL of hydrazine hydrate was added below the sample. The culture dish was heated at 50°C for 12 h to obtain the final piezoresistive sample.

#### Characterization and measurements

Compression experiments were performed on a compression testing machine (Shimadzu AGS-X 5N) at a strain rate of 5 mm/min. Before the test, the sample was compressed with an 80% compression level for 50 iterations. The Young's modulus was calculated throughout the first 40% of the compression. The energy loss coefficient was calculated by dividing the loss work by the compression work,  $W = \int_{\epsilon_1}^{\epsilon_2} \sigma d\epsilon$ , where  $W$  is the specific work;  $\epsilon_1$  and  $\epsilon_2$  are the initial and final compressive strain, respectively; and  $\sigma$  is the compressive stress.<sup>48</sup> The sensor was compressed by a compression testing machine (Shimadzu AGS-X 5N) while the resistance and current were measured using a Keithley 2000 digital multimeter. The sample was wrapped in two pieces of PET to form a sandwich structure. The PET was coated with silver nanoparticles by vacuum evaporation. The morphology of the aerogel was characterized by SEM (JSM-7800, Japan).

#### FEA simulations

FEA simulation was adopted to design the hyperbolic meta-structure and investigate the NPR effect of CPMs. A porous structure with a symmetric re-entrant skeleton and a disordered region (replaced with a rhombus) at the center part was established for the FEA models.<sup>19</sup> The S8R (eight nodes with a doubly curved thick shell with reduced integration) was selected as the element type in the meshing of the

-FEA models in the ABAQUS program. The constitutive model of the material in the FEM models was considered to be linear elastic with dimensionless parameters of  $E = 1$  and  $\nu = 0.3$ .

During compression, displacement was applied to the top boundary of the -FEA models and the bottom boundary was fixed. The NPR values were calculated as the ratio of lateral shrinking strain to vertical compressive strain. The effect of large geometric deformation was considered throughout the simulation. The compressive increment was 1% of the displacement in the compressive direction.

### SUPPLEMENTAL INFORMATION

Supplemental information can be found online at <https://doi.org/10.1016/j.matt.2022.02.022>.

### ACKNOWLEDGMENTS

This work was supported by the National Natural Science Foundation of China (51872146, 51633002, 11872063, and 11802302), the Municipal Natural Science Fund of Tianjin (20JCJQJC00010), MOST (2016YFA0200200), Fundamental Research Funds for the Central Universities of Nankai University (63191520), the Strategic Priority Research Program of the Chinese Academy of Sciences (XDB22040402), and USTC Research Funds of the Double First-Class Initiative (YD2480002002).

### AUTHOR CONTRIBUTIONS

Conceptualization, J.L.; methodology, J.L., H.-A.W., Y.C., X.S., and Y.Z.; investigation, X.S., Y.Z., X.F., P.W., and X.J.; simulation, Y.Z., and H.W.; writing and editing, J.L., H.W., X.S., and Y.Z.; supervision, J.L.

### DECLARATION OF INTERESTS

The authors declare no competing interests.

Received: July 23, 2021

Revised: November 7, 2021

Accepted: February 23, 2022

Published: March 18, 2022

### REFERENCES

1. Yu, K.-H., Beam, A.L., and Kohane, I.S. (2018). Artificial intelligence in healthcare. *Nat. Biomed. Eng.* 2, 719–731.
2. Pang, C., Koo, J.H., Nguyen, A., Caves, J.M., Kim, M.G., Chortos, A., Kim, K., Wang, P.J., Tok, J.B.H., and Bao, Z. (2015). Highly skin-conformal microhair sensor for pulse signal amplification. *Adv. Mater.* 27, 634–640.
3. Trung, T.Q., and Lee, N.E. (2016). Flexible and stretchable physical sensor integrated platforms for wearable human-activity monitoring and personal healthcare. *Adv. Mater.* 28, 4338–4372.
4. Ma, Y., Zhang, Y., Cai, S., Han, Z., Liu, X., Wang, F., Cao, Y., Wang, Z., Li, H., and Chen, Y. (2020). Flexible hybrid electronics for digital healthcare. *Adv. Mater.* 32, 1902062.
5. Zang, Y., Zhang, F., Di, C.-a., and Zhu, D. (2015). Advances of flexible pressure sensors toward artificial intelligence and health care applications. *Mater. Horiz.* 2, 140–156.
6. Yue, Y., Liu, N., Liu, W., Li, M., Ma, Y., Luo, C., Wang, S., Rao, J., Hu, X., and Su, J. (2018). 3D hybrid porous Mxene-sponge network and its application in piezoresistive sensor. *Nano Energy* 50, 79–87.
7. Guo, Y., Guo, Z., Zhong, M., Wan, P., Zhang, W., and Zhang, L. (2018). A flexible wearable pressure sensor with bioinspired microcrack and interlocking for full-range human-machine interfacing. *Small* 14, 1803018.
8. Zhang, S., Liu, H., Yang, S., Shi, X., Zhang, D., Shan, C., Mi, L., Liu, C., Shen, C., and Guo, Z. (2019). Ultrasensitive and highly compressible piezoresistive sensor based on polyurethane sponge coated with a cracked cellulose nanofibril/silver nanowire layer. *ACS Appl. Mater. Inter.* 11, 10922–10932.
9. Tian, H., Shu, Y., Wang, X.-F., Mohammad, M.A., Bie, Z., Xie, Q.-Y., Li, C., Mi, W.-T., Yang, Y., and Ren, T.-L. (2015). A graphene-based resistive pressure sensor with record-high sensitivity in a wide pressure range. *Sci. Rep.* 5, 1–6.
10. Shi, L., Li, Z., Chen, M., Qin, Y., and Wu, L. (2020). Quantum effect-based flexible and transparent pressure sensors with ultrahigh sensitivity and sensing density. *Nat. Commun.* 11, 1–9.
11. Pan, L., Chortos, A., Yu, G., Wang, Y., Isaacson, S., Allen, R., Shi, Y., Dauskardt, R., and Bao, Z. (2014). An ultra-sensitive resistive pressure sensor based on hollow-sphere microstructure

- induced elasticity in conducting polymer film. *Nat. Commun.* 5, 1–8.
12. Ma, Y., Yue, Y., Zhang, H., Cheng, F., Zhao, W., Rao, J., Luo, S., Wang, J., Jiang, X., and Liu, Z. (2018). 3D synergistical MXene/reduced graphene oxide aerogel for a piezoresistive sensor. *ACS Nano* 12, 3209–3216.
  13. Chen, Z., Hu, Y., Zhuo, H., Liu, L., Jing, S., Zhong, L., Peng, X., and Sun, R.-c. (2019). Compressible, elastic, and pressure-sensitive carbon aerogels derived from 2D titanium carbide nanosheets and bacterial cellulose for wearable sensors. *Chem. Mater.* 31, 3301–3312.
  14. Zhuo, H., Hu, Y., Chen, Z., Peng, X., Liu, L., Luo, Q., Yi, J., Liu, C., and Zhong, L. (2019). A carbon aerogel with super mechanical and sensing performances for wearable piezoresistive sensors. *J. Mater. Chem. A* 7, 8092–8100.
  15. Hu, Y., Zhuo, H., Luo, Q., Wu, Y., Wen, R., Chen, Z., Liu, L., Zhong, L., Peng, X., and Sun, R. (2019). Biomass polymer-assisted fabrication of aerogels from MXenes with ultrahigh compression elasticity and pressure sensitivity. *J. Mater. Chem. A* 7, 10273–10281.
  16. Sheng, L., Liang, Y., Jiang, L., Wang, Q., Wei, T., Qu, L., and Fan, Z. (2015). Bubble-decorated honeycomb-like graphene film as ultrahigh sensitivity pressure sensors. *Adv. Funct. Mater.* 25, 6545–6551.
  17. Jiang, Y., Liu, Z., Matsuhisa, N., Qi, D., Leow, W.R., Yang, H., Yu, J., Chen, G., Liu, Y., Wan, C., et al. (2018). Auxetic mechanical metamaterials to enhance sensitivity of stretchable strain sensors. *Adv. Mater.* 30, 1706589.
  18. Zhang, Q., Xu, X., Lin, D., Chen, W., Xiong, G., Yu, Y., Fisher, T.S., and Li, H. (2016). Hyperbolically patterned 3D graphene metamaterial with negative Poisson's ratio and superelasticity. *Adv. Mater.* 28, 2229–2237.
  19. Xu, X., Zhang, Q., Hao, M., Hu, Y., Lin, Z., Peng, L., Wang, T., Ren, X., Wang, C., and Zhao, Z. (2019). Double-negative-index ceramic aerogels for thermal superinsulation. *Science* 363, 723–727.
  20. Qiu, L., Huang, B., He, Z., Wang, Y., Tian, Z., Liu, J.Z., Wang, K., Song, J., Gengenbach, T.R., and Li, D. (2017). Extremely low density and super-compressible graphene cellular materials. *Adv. Mater.* 29, 1701553.
  21. Zhang, Q., Xu, X., Li, H., Xiong, G., Hu, H., and Fisher, T.S. (2015). Mechanically robust honeycomb graphene aerogel multifunctional polymer composites. *Carbon* 93, 659–670.
  22. Kashani, H., Ito, Y., Han, J., Liu, P., and Chen, M. (2019). Extraordinary tensile strength and ductility of scalable nanoporous graphene. *Sci. Adv.* 5, eaat6951.
  23. Qiu, L., Bulut Coskun, M., Tang, Y., Liu, J.Z., Alan, T., Ding, J., Truong, V.T., and Li, D. (2016). Ultrafast dynamic piezoresistive response of graphene-based cellular elastomers. *Adv. Mater.* 28, 194–200.
  24. Engheta, N., and Ziolkowski, R.W. (2006). *Metamaterials: Physics and Engineering Explorations* (John Wiley & Sons), p. 2006.
  25. Liu, R., Cui, T.J., and Smith, D.R. (2010). General theory on artificial metamaterials. In *Metamaterials*, T.J. Cui, D. Smith, and R. Liu, eds. (Springer), pp. 49–59.
  26. Anasori, B., Lukatskaya, M.R., and Gogotsi, Y. (2017). 2D metal carbides and nitrides (MXenes) for energy storage. *Nat. Rev. Mater.* 2, 16098.
  27. Fan, X., Yang, Y., Shi, X., Liu, Y., Li, H., Liang, J., and Chen, Y. (2020). A MXene-based hierarchical design enabling highly efficient and stable solar-water desalination with good salt resistance. *Adv. Funct. Mater.* 30, 2007110.
  28. Kolken, H.M., and Zadpoor, A. (2017). Auxetic mechanical metamaterials. *RSC Adv.* 7, 5111–5129.
  29. Zadpoor, A.A. (2016). Mechanical metamaterials. *Mater. Horiz.* 3, 371–381.
  30. Lee, J.H., Singer, J.P., and Thomas, E.L. (2012). Micro-/nanostructured mechanical metamaterials. *Adv. Mater.* 24, 4782–4810.
  31. Hou, X., and Silberschmidt, V.V. (2015). Metamaterials with negative Poisson's ratio: a review of mechanical properties and deformation mechanisms. *Mech. Adv. Mater.* 155–179.
  32. Lipatov, A., Alhabeab, M., Lukatskaya, M.R., Boson, A., Gogotsi, Y., and Sinitskii, A. (2016). Effect of synthesis on quality, electronic properties and environmental stability of individual monolayer Ti3C2 MXene flakes. *Adv. Electron. Mater.* 2, 1600255.
  33. Qian, X., Fan, X., Peng, Y., Xue, P., Sun, C., Shi, X., Lai, C., and Liang, J. (2021). Polysiloxane cross-linked mechanically stable MXene-based lithium host for ultrastable lithium metal anodes with ultrahigh current densities and capacities. *Adv. Funct. Mater.* 31, 2008044.
  34. Lin, J., Siddiqui, J.A., and Ottenbrite, R.M. (2001). Surface modification of inorganic oxide particles with silane coupling agent and organic dyes. *Polym. Adv. Tech.* 12, 285–292.
  35. Zhao, J., Yang, Y., Yang, C., Tian, Y., Han, Y., Liu, J., Yin, X., and Que, W. (2018). A hydrophobic surface enabled salt-blocking 2D Ti3C2 MXene membrane for efficient and stable solar desalination. *J. Mater. Chem. A* 6, 16196–16204.
  36. Kumar, S., Lei, Y., Alshareef, N.H., Quevedo-Lopez, M., and Salama, K.N. (2018). Biofunctionalized two-dimensional Ti3C2 MXenes for ultrasensitive detection of cancer biomarker. *Biosens. Bioelectron.* 121, 243–249.
  37. Cao, W.-T., Feng, W., Jiang, Y.-Y., Ma, C., Zhou, Z.-F., Ma, M.-G., Chen, Y., and Chen, F. (2019). Two-dimensional MXene-reinforced robust surface superhydrophobicity with self-cleaning and photothermal-actuating binary effects. *Mater. Horiz.* 6, 1057–1065.
  38. Zhu, C., Han, T.Y.-J., Duoss, E.B., Golobic, A.M., Kuntz, J.D., Spadaccini, C.M., and Worsley, M.A. (2015). Highly compressible 3D periodic graphene aerogel microlattices. *Nat. Commun.* 6, 1–8.
  39. Worsley, M.A., Kucheyev, S.O., Satcher, J.H., Jr., Hamza, A.V., and Baumann, T.F. (2009). Mechanically robust and electrically conductive carbon nanotube foams. *Appl. Phys. Lett.* 94, 073115.
  40. Yu, Z.L., Qin, B., Ma, Z.Y., Huang, J., Li, S.C., Zhao, H.Y., Li, H., Zhu, Y.B., Wu, H.A., and Yu, S.H. (2019). Superelastic hard carbon nanofiber aerogels. *Adv. Mater.* 31, 1900651.
  41. Yin, B., Liu, X., Gao, H., Fu, T., and Yao, J. (2018). Bioinspired and bristled microparticles for ultrasensitive pressure and strain sensors. *Nat. Commun.* 9, 1–8.
  42. Jian, M., Xia, K., Wang, Q., Yin, Z., Wang, H., Wang, C., Xie, H., Zhang, M., and Zhang, Y. (2017). Flexible and highly sensitive pressure sensors based on bionic hierarchical structures. *Adv. Funct. Mater.* 27, 1606066.
  43. Park, J., Lee, Y., Hong, J., Ha, M., Jung, Y.D., Lim, H., Kim, S.Y., and Ko, H. (2014). Giant tunneling piezoresistance of composite elastomers with interlocked microdome arrays for ultrasensitive and multimodal electronic skins. *ACS Nano* 8, 4689–4697.
  44. Wang, X., Gu, Y., Xiong, Z., Cui, Z., and Zhang, T. (2014). Silk-molded flexible, ultrasensitive, and highly stable electronic skin for monitoring human physiological signals. *Adv. Mater.* 26, 1336–1342.
  45. Wang, K., Lou, Z., Wang, L., Zhao, L., Zhao, S., Wang, D., Han, W., Jiang, K., and Shen, G. (2019). Bioinspired interlocked structure-induced high deformability for two-dimensional titanium carbide (MXene)/natural microcapsule-based flexible pressure sensors. *ACS Nano* 13, 9139–9147.
  46. Hu, H., Zhao, Z., Wan, W., Gogotsi, Y., and Qiu, J. (2013). Ultralight and highly compressible graphene aerogels. *Adv. Mater.* 25, 2219–2223.
  47. Liang, J., Huang, Y., Zhang, L., Wang, Y., Ma, Y., Guo, T., and Chen, Y. (2009). Molecular-level dispersion of graphene into poly (vinyl alcohol) and effective reinforcement of their nanocomposites. *Adv. Funct. Mater.* 19, 2297–2302.
  48. Si, Y., Wang, X., Dou, L., Yu, J., and Ding, B. (2018). Ultralight and fire-resistant ceramic nanofibrous aerogels with temperature-invariant superelasticity. *Sci. Adv.* 4, eaas8925.